Research Article Vol. 31, No. 4 / 13 Feb 2023 / Optics Express 5777
Optics EXPRESS

Theoretical modeling and simulation of fiber Bragg grating sensor interrogator based on linear variable filter

YI LIU,[1,2,*] ZHAOYI LIU,[1,2] ANYI HUANG,[1] JIE WANG,[2] AND CHENG XIN[3]

[1]School of Mechanical and Electronic Engineering, Wuhan University of Technology, Wuhan 430070, China
[2]Shaoxing Institute for Advanced Research, Wuhan University of Technology, Shaoxing 312300, China
[3]Photonics Research Center, Department of Electrical Engineering, Hong Kong Polytechnic University, 11 Yuk Choi Rd, Hung Hom, Hong Kong SAR 999077, China
*Wgdliuyi2001@whut.edu.cn

Abstract: With the increasing frequency of aviation accidents in recent years, aircraft safety has received increasing attention. Aircraft operating condition detection is an important part of aviation safety. Fiber Bragg grating (FBG) sensors, with their excellent characteristics, enable online monitoring of aircraft operating conditions. However, the application of FBG sensors in aviation is currently limited because it is difficult for FBG sensor interrogators to meet the requirements of small size, light weight, and good vibration resistance in the aviation field. Therefore, this paper proposes a linear variable filter (LVF)-based FBG sensor interrogator to meet the requirements. An optical model of the interrogator is established. The parameters which determine the performances of the interrogator are analyzed and the design criteria are discussed. According to the requirements in the aviation field, the optical system of the interrogator is designed. The simulation results show that the LVF-based FBG sensor interrogation system has a bandwidth range of *90* nm (*1505* nm-*1595* nm), a resolution of *2* pm, and a capacity of *15* FBG sensors.

1. Introduction

Fiber Bragg grating (FBG) sensors have remarkable advantages over electrical sensors, e.g., they are more sensitive, can be used in extreme conditions, and are immune to electromagnetic interference. FBG sensors can also be used to detect various physical properties such as vibration [1], acceleration [2], pressure [3], temperature [4], and humidity [5]. Owing to the above advantages, FBG sensors are widely used in civil engineering [6], medical [7], aviation [8,9] fields. Particularly in the aviation field, compared with traditional sensors, FBG sensors enable not only real-time monitoring but also the detection of a wide range of physical quantities. Therefore, the application of FBG sensors to the aviation field can simplify detection systems and improve their timeliness. Ciminello et al. [10] used FBG sensors to achieve real-time monitoring of aircraft structural safety, and Yan et al. [11] used them for precise temperature management in aircraft cabins. These confirm that FBG sensors have wide-ranging applications in the aviation field. The unique working environment of the aviation field necessitates light weight and anti-vibration requirements for aviation instruments. However, the current FBG sensor interrogation systems cannot meet these requirements.

An FBG sensor interrogator is a spectral identification instrument whose main function is to identify the wavelength of the light reflected from FBG sensors. Common wavelength interrogation methods are the wavelength matching, edge filter, interferometer, spectral imaging, and tunable laser source methods. The wavelength matching method [12,13] uses a reference FBG or a Fabry-Perot (F-P) cavity to track the wavelength changes of FBG sensors. Piezoelectric

#475654 https://doi.org/10.1364/OE.475654
Journal © 2023 Received 14 Sep 2022; revised 13 Dec 2022; accepted 3 Jan 2023; published 2 Feb 2023

Optics EXPRESS

ceramics influence the performance of this method. Moreover, an instrument based on this method has a large mass and poor vibration resistance. The edge filter method [14] uses a linear filter, whose output light intensity varies linearly with the wavelength of the input light. This method has a high interrogation speed but difficulty in multiplexing. The interferometer method [15] converts a wavelength change of FBG sensors into a phase change. It has high sensitivity but poor vibration resistance. The spectral imaging method [16] uses a dispersion component and a line array image sensor to sample the spectrum reflected from FBG sensors in parallel. This method has a moderate interrogation speed. However, it requires strict control of the geometric position relationship between the components. Consequently, an instrument of this method has poor vibration resistance and a large mass. The tunable laser source method [17,18] obtains the wavelength of the light reflected from FBG sensors by sweeping the laser wavelength. This method has a high signal-to-noise ratio but a low interrogation speed. Based on the above analysis, the existing interrogation methods do not perfectly meet the requirements of light weight and vibration resistance in the aviation field. Therefore, establishing a new interrogation method to solve the limited application problem of FBG sensors in the aerospace field is necessary.

A linear variable filter (LVF) is a thin-film dispersion component whose spectral properties vary along its length. It can map the spectral distribution of an incident light to the spatial distribution of the transmitted light. It has been widely used in spectrometers [19–21] and hyperspectral imaging [22–24]. Because an LVF can be placed directly on the window of a detector without a focusing lens and the focusing distance, LVF-based instruments are light, small, and vibration-resistant. Amdi et al. [19] applied an LVF to the design of a micro spectrometer to achieve a resolution of *0.7* nm in the visible range. A micro spectrometer has the advantages of high luminous flux, good vibration resistance, small size, and light weight compared with the conventional spectrometer. Piegari et al. [23] applied an LVF to the design of a spectral camera, enabling it to meet the requirements of working in the space field and accomplishing the detection of the surface of the Earth. Given the above advantages, an LVF can well meet the requirements for instruments in the aviation field; however, the research on LVF-based FBG sensor interrogation systems has been neither not systematic nor comprehensive.

Previous studies [25–27] investigated and experimentally verified interrogators based on an LVF for a single FBG sensor. However, they did not consider an interrogator for multi-FBG sensors and did not provide the design criteria of FBG sensor interrogators based on an LVF. With the maturity of the LVF fabrication process [28,29], LVF-based interrogation methods have achieved increasingly prominent advantages in the aviation field. Therefore, a systematic and comprehensive investigation of this type of interrogation system is conducted in this study. The considered interrogation system consists of three components: a collimating lens, an LVF, and a line array image detector. The relationships between the performances of this type of interrogation system and the optical properties of its components are analyzed. Moreover, a multi-FBG sensor-based interrogation model is developed, based on which the design criteria of the LVF and the collimating lens are established. Moreover, an LVF-based FBG sensor interrogation system is designed. The simulation results show that its bandwidth range is increased from *70* nm to *90* nm, its resolution is improved from *3.5* pm to *2* pm, and the capacity of FBG sensors is increased from *1* to *15* compared to those of a previous design [30].

2. Principles of interrogation

The considered LVF-based FBG sensor sensing system consists of an amplified spontaneous emission (ASE) laser source (broadband light source), a circulator, an FBG sensor array, and an interrogation system, as shown in Fig. 1(a). The broadband light emitted from the ASE laser source passes through the circulator and is incident on the FBG sensor array. Each FBG sensor reflects a narrowband light of a particular wavelength. Each narrowband light reflected by the FBG sensors passes through the circulator again and enters the interrogation system. As shown

Optics EXPRESS

in Fig. 1(b), the interrogation system includes three parts: a collimating lens, an LVF, and a line array image detector. Each narrow-band light is emitted from a pigtail, collimated by the lens, and then is incident vertically on the LVF. After filtering by the LVF, the narrowband lights with different wavelengths are located at different positions on the line array image detector. Thus, the positions of the wave peaks can be used to calculate the wavelengths of the lights reflected by the FBG sensors. Subsequently, the external physical properties encoded by the wavelengths of the lights reflected by the FBG sensors can be detected.

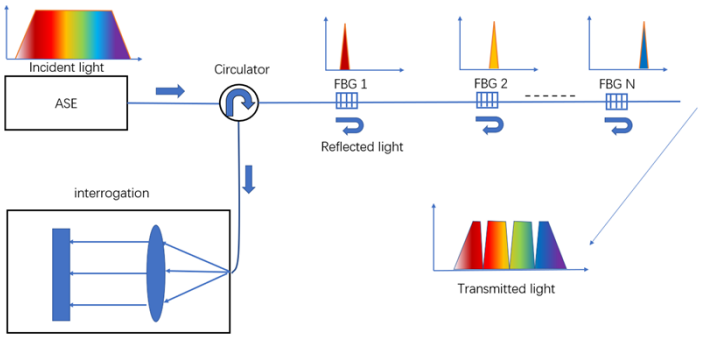

(a)

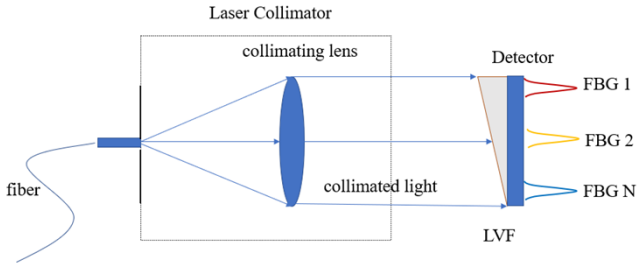

(b)

Fig. 1. (a) Schematic of FBG sensor sensing system based on LVF; (b) Schematic of interrogation system in (a).

The narrowband lights reflected by the FBG sensors, as shown in Fig. 1(b), form wave peaks of a specific width on the detector. From the principle of wave peak superposition, when wave peaks are extremely wide, the wave peaks at adjacent positions are degraded into a single wave peak. Owing to this phenomenon, the detector cannot correctly identify the positions of the wave peaks. Therefore, the width of the wave peaks should be designed to avoid degradation.

As shown in Fig. 1(b), the LVF is a thin-film component; therefore, it can greatly reduce the total mass of the instrument. Moreover, the LVF can be placed directly on the window of the line array image detector, which not only reduces the spatial distance but also improves the vibration resistance. Therefore, the LVF-based FBG sensor interrogation system has the advantages of light weight, small size, and good vibration resistance.

Optics EXPRESS

3. Model and design of an LVF-based interrogator for FBG sensors

3.1. Model and design of an LVF

As shown in Fig. 2, the LVF is an F-P type of interference filter, which can be theoretically modeled and designed using the F-P interference theory. Therefore, the wavelength transmission characteristics of the LVF can be expressed as

$$m\lambda = 2nd \tag{1}$$

where m is the spectral order, λ is the wavelength of the transmitted light, n is the refractive index of the resonant cavity, and d is the thickness of the resonant cavity. The wavelength of the transmitted light of the LVF is determined by the thickness of the resonant cavity, as expressed in Eq. (1). Because the resonant cavity thickness of the LVF increases linearly along its length direction, white light shows a dispersion distribution when passing through the LVF, as shown in Fig. 2. However, under the influence of the spectral order, m, the transmitted light is not monochromatic but composite consisting of a series of discrete wavelengths. This phenomenon is called ambiguity of wavelength interrogation.

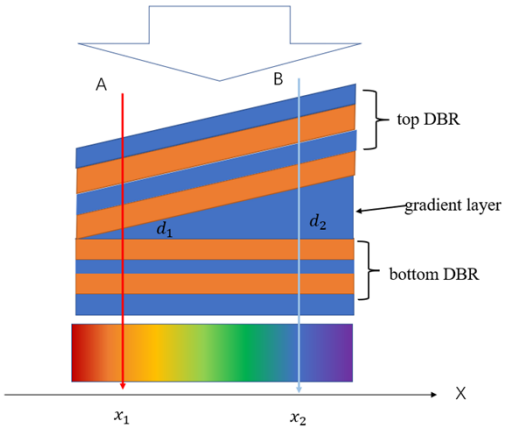

Fig. 2. Schematic of structure of LVF. LVF consists of three parts: top distributed Bragg reflector (DBR), middle gradient layer, and bottom DBR.

As shown in Fig. 2, A and B are two points in the length direction of the LVF, and their positions on the x-axis are x_1 and x_2, respectively. The resonant cavity thicknesses at A and B are d_1 and d_2, respectively. Assume that the wavelengths of the transmitted light with spectral order m at A and B are λ_1 and λ_2, respectively.

$$m\lambda_1 = 2nd_1 \tag{2}$$

$$m\lambda_2 = 2nd_2 \tag{3}$$

To eliminate ambiguity in the region between A and B, the wavelengths of the transmitted light between A and B must be in the same spectral order. Thus, the transmitted light wavelength with spectral order $m + 1$ at B must be outside the bandwidth range between A and B.

$$2nd_2 = (m + 1)\lambda_3 \tag{4}$$

$$\lambda_3 < \lambda_1 \tag{5}$$

Optics EXPRESS

where λ_3 is the transmitted light wavelength with spectral order $m+1$ at B. Incorporating Eqs. (3) and (4) into Eq. (5), we obtain

$$\lambda_2 - \lambda_1 < \frac{\lambda_2}{m+1} \tag{6}$$

Extending Eq. (3) to the entire bandwidth range, $\lambda_{\max}$ and $\lambda_{\min}$ denoting the upper and lower limits of the entire bandwidth range, respectively, yield

$$\lambda_{\max} - \lambda_{\min} < \frac{\lambda_{\max}}{m+1} \tag{7}$$

Equation (7) expresses the design criterion of the spectral order, m, is proposed. As mentioned above, if the width of the wave peaks is extremely wide, the adjacent wave peaks will be degraded into a single wave peak. Thus, for a detector having a fixed length and wave peaks of certain widths, the number of wave peaks that can be interrogated without degradation is limited, and the width of the wave peaks affects the number of FBG sensors that can be interrogated.

The relationships between the width of the wave peaks and the optical properties of the LVF are discussed. The spectral transmittance of the LVF is as follows [31]:

$$T = \frac{1}{1 + F\sin^2(\theta)} \tag{8}$$

$$\theta = \frac{nd}{\lambda} 2\pi \cos(\varphi) \tag{9}$$

where T is the spectral transmittance, λ is the wavelength of the incident light, and φ is the incident angle. F is the coefficient of fineness, which depends on the reflectance of the reflector as follows: $F = 4R/(1-R)^2$.

As shown in Fig. 2, the transmitted light wavelength of the LVF varies linearly along the x-axis. Therefore, the relationship between the wavelength and the position can be expressed by a linear function.

$$\lambda_x = \lambda_0 + g(x - \frac{L}{2}) \tag{10}$$

$$g = \frac{\lambda_{\max} - \lambda_{\min}}{L} \tag{11}$$

$$\lambda_0 = \frac{\lambda_{\max} + \lambda_{\min}}{2} \tag{12}$$

where λ_x is the wavelength of the transmitted light at position x, g is the linear dispersion coefficient, L is the length of the detector (in this study, the length of the linear image detector is the length of the LVF), and λ_0 is the wavelength of the transmitted light at the middle position of the LVF. The thickness of the resonant cavity at position x can be obtained from Eq. (1) as follows:

$$d_x = \frac{m\lambda_x}{2n} \tag{13}$$

In the case of vertical illumination ($\varphi = 0°$), substituting Eqs. (9) and (13) into Eq. (8) yields

$$T = \frac{1}{1 + F\sin^2(m\pi \frac{\lambda_x}{\lambda})} \tag{14}$$

The above equation shows that the spectral transmittance of the LVF is not only related to the wavelength of the incident light but also to the position on the x-axis. Substituting Eq. (10) into Eq. (14) yields

$$T_{LVF} = \frac{1}{1 + F\sin^2(\pi \frac{m(\lambda_0 + g(x - L/2))}{\lambda})} \tag{15}$$

where T_{LVF} is the spectral transmittance of the LVF.

Optics EXPRESS

The light reflected by an FBG sensor is a narrowband light with a certain bandwidth. It is assumed that the spectral function of a light reflected by a FBG sensors is $spec(\lambda_{FBG}, \lambda)$, where λ_{FBG} denotes the central wavelength of this light. The spatial distribution function of the incident light is denoted as: $spa(x)$. As shown in Fig. 3, the incident light is filtered by the LVF and then received by the detector. The distribution of the transmitted light is

$$I_{out}(x) = \int spa(x)spec(\lambda_{FBG}, \lambda)T_{LVF}(x, \lambda)d\lambda \tag{16}$$

where $I_{out}(x)$ denotes the intensity distribution of the transmitted light. Equation (16) is the interrogation model developed in this study.

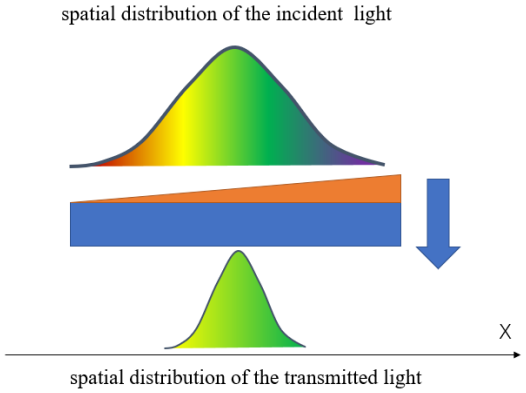

Fig. 3. Schematic diagram of the interrogation model.

Assuming that the light reflected by each FBG sensor is monochromatic and has a uniform spatial distribution,

$$spec(\lambda_{FBG}, \lambda) = \delta(\lambda - \lambda_{FBG}) \tag{17}$$

$$spa(x) = 1 \tag{18}$$

where $\delta(\lambda)$ denotes a pulse function. Thus, Eq. (16) can be simplified as follows:

$$I_{out}(x) = \int T_{LVF}(x, \lambda)\delta(\lambda - \lambda_{FBG})d\lambda = \frac{1}{1 + F\sin^2(\pi\frac{m(\lambda_0 + g(x - L/2))}{\lambda})} \tag{19}$$

The calculation results of Eq. (19) are shown in Fig. 4, where the parameters are as follows: $\lambda_0 = 1550\ nm$, $\lambda_{FBG} = 1550\ nm$, $m = 4$, $R = 0.9$, $L = 6\ mm$, $g = 15\ nm/mm$.

The lights reflected by FBG sensors form wave peaks of a certain width on the detector, as shown in Fig. 4(a). For the wave peak shown in Fig. 4(a), the distance between the points whose heights are half of the maximum height is defined as the full width at half maxima (FWHM). In this study, we use the FWHM to denote the wave peak width.

From Eq. (19), the maximum intensity of the transmitted light is *1*. Therefore, the points whose heights are half of the maximum height are obtained by solving the following equation:

$$T_{LVF}(x_h, \lambda_{FBG}) = \frac{1}{1 + F\sin^2(\pi\frac{m(\lambda_0 + g(x_h - L/2))}{\lambda_{FBG}})} = 0.5 \tag{20}$$

where x_h is the coordinate of the point with an intensity of *0.5* on the x-axis. Solving Eq. (20) yields

$$x_{h1} = \frac{L}{2} - \frac{\lambda_0}{g} + \frac{\lambda_{FBG}}{g} - \frac{\lambda_{FBG}\arcsin(\frac{1}{\sqrt{F}})}{m\pi g} \tag{21}$$

Optics EXPRESS

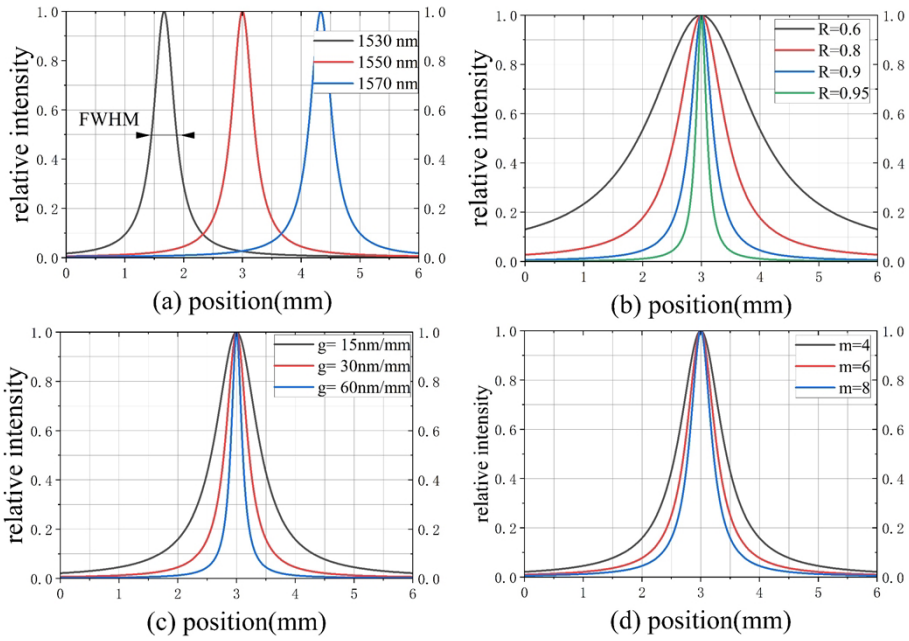

Fig. 4. (a) Intensity distribution of transmitted light when wavelengths of light reflected by FBG sensors are *1530* nm, *1550* nm, and *1570* nm, respectively; (b)Intensity distributions of transmitted light when reflectivity values of reflector are *0.6*, *0.8*, *0.9*, and *0.95*, respectively; (c) Intensity distributions of transmitted light when linear dispersion coefficient values of LVF are *15* nm/mm, *30* nm/mm, and *60* nm/mm, respectively; (d) Intensity distributions of transmitted light when spectral orders of LVF are *4*, *6*, and *8*, respectively.

$$x_{h2} = \frac{L}{2} - \frac{\lambda_0}{g} + \frac{\lambda_{FBG}}{g} + \frac{\lambda_{FBG}\arcsin(\frac{1}{\sqrt{F}})}{m\pi g} \tag{22}$$

where x_{h1} *and* x_{h2} are the coordinates of the point with an intensity of *0.5* on the X-axis, respectively. Therefore, the width of the wave peak of the transmitted light is expressed by the following equation:

$$FWHM_{mon} = |x_{h1} - x_{h2}| \tag{23}$$

Substituting Eqs. (21) and (22) into Eq. (23) yields

$$FWHM_{\text{mon}} = \frac{2\arcsin(1/\sqrt{F})}{m\pi g}\lambda_{FBG} \tag{24}$$

where $FWHM_{\text{mon}}$ is the peak width of the transmitted light when the incident light is monochromatic and has a uniform spatial distribution. From Eq. (24), the wave peak width of the transmitted light decreases with the increase in F. Moreover, F is positively correlated with the reflectivity of the reflector, R. Therefore, the wave peak width of the transmitted light decreases with the increase in the reflectivity of the reflector, R, as shown in Fig. 4(b). Figure 4(c) and (d) show the relationships between the wave peak width of the transmitted light with the linear dispersion coefficient, g, and the spectral order, m, respectively. The wave peak width of the transmitted light decreases as g and m increase. Thus, the desired wave peak width can be obtained by choosing the appropriate coefficient of fineness F, spectral order m, and linear dispersion coefficient g.

Optics EXPRESS

The Riley criterion states that no degradation occurs when the distance between two wave peaks is greater than their widths. Thus, the constraint on the wave peak width is as follows:

$$\frac{L}{Num} \geq FWHM_{mon} \tag{25}$$

where L is the detector length and Num is the capacity of the FBG sensors. Equations (25) and (7) define the design criteria of the LVF.

For the all-dielectric LVF, as shown in Fig. 2, the top and bottom distributed Bragg reflectors (DBRs) are composed of multiple layers of dielectric materials. Moreover, the high reflectivity is limited to a specific bandwidth. Thus, the wave peaks of the transmitted light can only be observed in the high-reflectivity bandwidth of the DBRs. Therefore, the bandwidth range of the LVF designed in this study is also limited by the maximum reflection bandwidth of the DBRs, as expressed in the following equation:

$$\frac{\Delta\lambda}{\lambda_0} = \frac{4}{\pi}\arcsin\left(\frac{n_2 - n_1}{n_2 + n_1}\right) \tag{26}$$

where $\Delta\lambda$ is the maximum reflection bandwidth of the DBRs, λ_0 is the design wavelength of the DBRs, n_2 and n_1 are the refractive indexes of the high- and the low-refractive index materials of the DBRs, respectively. For the interrogation system, the bandwidth range must not exceed $\Delta\lambda$.

The film system design of the LVF is $sub/(HL)^N(2mH)(LH)^N/air$, where H denotes the quarter wavelength optical thickness of the high-refractive index material, L denotes the quarter wavelength optical thickness of the low-refractive index material, m is the spectral order, and N is the number of layers of the high-refractive index materials in the DBRs. The reflectivity of the DBRs is [31]:

$$Y = \frac{{n_1}^{2N}}{{n_2}^{2N}} n_g \tag{27}$$

$$R = (n_2 - Y)^2/(n_2 + Y)^2 \tag{28}$$

where n_g is the refractive index of the substrate and R is the reflectivity of the DBRs. Because R is determined by N, as expressed in Eqs. (27) and (28), the appropriate N can be chosen based on the desired m and R. The relationship between N and $FWHM_{mon}$ can be obtained by substituting Eqs. (27) and (28) into Eq. (24).

$$FWHM_{mon} = 2\lambda_{FBG}\frac{\arcsin\left(\frac{n_a - n_b}{\sqrt{2}n_a}\right)}{gm\pi} \tag{29}$$

$$n_a = n_2 - n_g(n_1/n_2)^{2N} \tag{30}$$

$$n_b = n_2 + n_g(n_1/n_2)^{2N} \tag{31}$$

where λ_{FBG} is the central wavelength of the light reflected by FBG sensors.

For the top and bottom DBRs of the LVF, the reference wavelength is λ_0, which is consistent with the transmitted light wavelength in the middle position of the LVF. Thus, the thickness of a single layer in a DBR can be expressed as followings:

$$d_H = \frac{\lambda_0}{4n_1} \tag{32}$$

$$d_L = \frac{\lambda_0}{4n_2} \tag{33}$$

where d_H and d_L are the actual thicknesses of the single layers of high- and low-refractive index materials in a DBR, respectively. However, because the wavelengths of the transmitted light

Optics EXPRESS

increase linearly along the x-axis direction in the resonant cavity, as expressed in Eq. (10), the thickness of the resonant cavity is

$$d_x = \frac{m\lambda_x}{2n_1} = \frac{m(g(x - L/2) + \lambda_0)}{n_1} \tag{34}$$

where d_x is the thickness of the resonant cavity at position x. λ_x is the wavelength of transmitted light at position x. The spatial taper angle of the LVF is expressed as

$$\theta_{LVF} \approx \tan\theta_{LVF} = \frac{d_{\max} - d_{\min}}{L} \tag{35}$$

where θ_{LVF} is the taper angle of the LVF, $d_{\min}$ is the minimum resonant cavity thickness, and $d_{\max}$ is the maximum resonant cavity thickness.

The system parameters of the interrogation system designed in this study are listed in Table 1. For the selection of the high- and low-refractive index materials of the DBR, satisfying the transparency in the bandwidth range and the high difference between the reflective indexes of the two types of dielectric materials is necessary. Thus, the high- and low-refractive index materials were chosen as Ta_2O_5 and SiO_2, respectively. Substituting the refractive indexes of the dielectric materials into Eq. (26), we obtain $\Delta\lambda = 370\ nm$. Thus, the bandwidth range must not exceed *370* nm. As summarized in Table 1, a bandwidth range of *90* nm is chosen to meet the maximum reflection bandwidth limit of the DBRs.

Table 1. System parameters of interrogator

System Parameters	Values
Bandwidth range	1505 nm-1595 nm
Central wavelength λ_0	1550 nm
Detector length L	6 mm
The initial design of the film system	$sub/(HL)^N(2mH)(LH)^N/air$[a]
Grating capacity	20

[a]m is spectral order of LVF, and N is the number of layers of the high-refractive materials in DBR.

Substituting the operating range of *90* nm (*1505* nm-*1595* nm) into Eq. (7) yields $m \leq 16$. The LVF can be viewed as consisting of numerous F-P filters, and its spectral order, m, needs to be constrained by the design constraint of the F-P filter [31]: $m \leq 4$. When the spectral order exceeds four, the scattering in the resonant cavity layer increases significantly, resulting in a significant decrease in the spectral transmittance of the filter. It is also known from Eq. (24) that increasing the spectral order reduces the wave peak width of the transmitted light, and thus, increases the capacity of FBG sensors. In this study, the spectral order, m, is chosen as *4* by combining the above two constraints.

The interrogation system is designed to achieve a capacity of *20* FBG sensors. From Eq. (25), we obtain $FWHM_{mon} = 0.3\ mm$. Because the bandwidth range varies in a small range around the central wavelength of the bandwidth range,

$$\lambda_{FBG} \approx \lambda_0 \tag{36}$$

where λ_0 is the central wavelength of the bandwidth range. Introducing Eq. (36) into Eq. (29) yields

$$FWHM_{mon} = 2\lambda_0 \frac{\arcsin(\frac{n_a - n_b}{\sqrt{2}n_a})}{gm\pi} \tag{37}$$

Taking $FWHM_{mon} = 0.3\ mm$ into the above equation, we obtain $N = 5$. The thickness of the layers of each DBR is obtained by taking $\lambda_0 = 1550\ nm$ into Eq. (32) and (33), as expressed in

Optics EXPRESS

Table 2. Using the bandwidth range of "*1505* nm-*1595* nm" into Eq. (11) and (34), we obtain that the thickness of the resonant cavity increases linearly along the x-axis from *1433.33* nm at the leftmost end to *1519.05* nm at the rightmost end, as listed in Table 2. From Eq. (35), we obtain that $\theta_{LVF} = 1.42 \times 10^{-5} rad$.

Table 2. Thicknesses of layers of LVF

Layer	Material	Thickness (nm)	Loop
Substrate	Glass	-	-
1	Ta_2O_5	184.52	5
2	SiO_2	268.35	5
3	Ta_2O_5	1433.33-1519.05	1
4	SiO_2	184.52	5
5	Ta_2O_5	268.35	5

3.2. Model and design of collimating lens

When the light reflected by the FBG sensors is not incident vertically on the LVF ($\varphi \neq 0°$), Eq. (19) is changed to

$$I_{out}(x) = \frac{1}{1 + F\sin^2(\pi \frac{m(\lambda_0 + g(x - L/2)}{\lambda} \cos(\varphi))} \tag{38}$$

where φ is the incidence angle. Figure 5 shows the results calculated results using Eq. (38). The wave peaks of the transmitted light shift in the positive x direction as the incident angle increases. Thus, the lights of the same wavelength but with different incident angles appear at different positions after filtering through the LVF. This phenomenon impairs the ability of the LVF to identify wavelengths and causes errors in the wavelength interrogation.

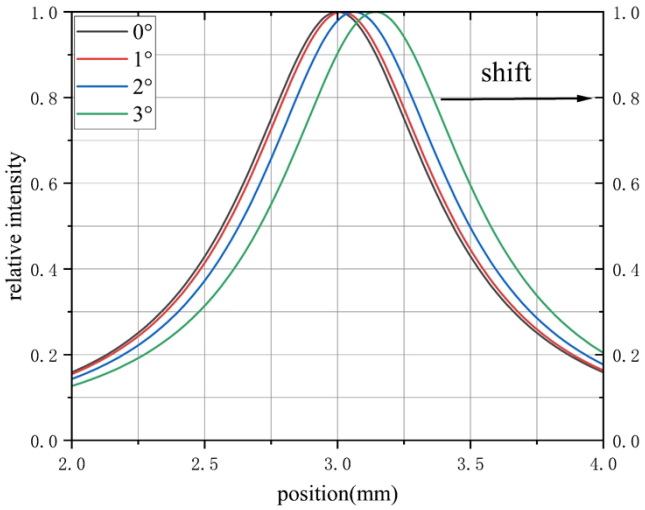

Fig. 5. Light intensity distributions of transmitted light with wavelength of 1550 nm when angles of incidence are 0°, 1°, 2° and 3°, respectively.

The lights reflected by the FBG sensors are diverging light. Thus, a lens is required, as shown in Fig. 1(b), to collimate the lights reflected by the FBG sensors before they are incident on

Optics EXPRESS

the LVF. Given the difficulty of fabrication, a spherical lens was chosen for the design of the collimating lens.

To ensure that each pixel point of the detector receives signals, the incident light must cover the entire detector area.

$$w \geq L/2 \tag{39}$$

where w is the radius of the spot incident on the LVF and L is the length of the linear image detector. The LVF should be placed at the beam waist position of the image Gaussian beam, as shown in Fig. 6, to maximize energy utilization and minimize the divergence angle of the light incident on the LVF.

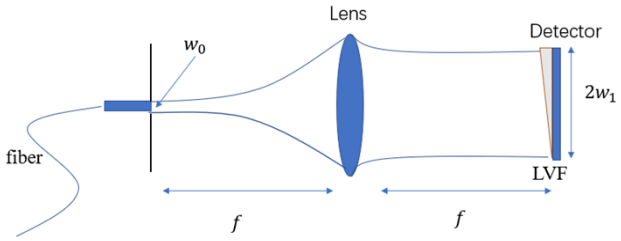

Fig. 6. Schematic of working principle of collimating lens.

The light emitted from the pigtail to the LVF is a Gaussian beam with a beam waist, w_0, and the position of the pigtail is the position of the beam waist. As shown in Fig. 6, the pigtail is placed at the object focal point, and the distance from the collimating lens is the focal length, f. Subsequently, the position of the image focal point is where the image Gaussian beam waist is located, and the radius of the beam waist is w_1. The transmission matrix of the Gaussian beam is as follows:

$$\frac{1}{f} = (n-1)\left(\frac{1}{R_1} - \frac{1}{R_2}\right) \tag{40}$$

$$\begin{bmatrix} A & B \\ C & D \end{bmatrix} = \begin{bmatrix} 1 & f \\ 0 & 1 \end{bmatrix}\begin{bmatrix} 1 & 0 \\ -\frac{1}{f} & 1 \end{bmatrix}\begin{bmatrix} 1 & f \\ 0 & 1 \end{bmatrix} = \begin{bmatrix} 0 & \frac{1}{(n_c-1)(\frac{1}{R_1}-\frac{1}{R_2})} \\ -(\frac{1}{R_1}-\frac{1}{R_2})(n_c-1) & 0 \end{bmatrix} \tag{41}$$

where f is the focal length of the lens, R_1 and R_2 are the radii of curvature of the first and second sides of the lens, respectively, and n_c is the refractive index of the lens glass.

$$q_0 = i\frac{\pi {w_0}^2}{\lambda_0} \tag{42}$$

$$q_1 = i\frac{\pi {w_1}^2}{\lambda_0} \tag{43}$$

$$q_1 = \frac{Aq_0 + B}{Cq_0 + D} \tag{44}$$

where q_0 and q_1 is the q-parameters at the object and image focal point, respectively. λ_0 is the wavelength of the Gaussian beam. w_0 and w_1 are the beam waists of the object and image Gaussian beams, respectively. In this study, the image beam waist is the radius of the light spot

Optics EXPRESS

incident on the LVF. Equations (40)–(44), can be simultaneously obtained

$$w_1 = \frac{\lambda_0}{\pi w_0(\frac{1}{R_1} - \frac{1}{R_2})(n-1)} = \frac{\lambda_0}{\pi w_0} f \tag{45}$$

$$f = \frac{\pi w_0 w_1}{\lambda_0} \tag{46}$$

From Eq. (46), it can be seen that the beam waist of the image Gaussian beam is proportional to the focal length of the lens. Thus, only selecting a suitable focal length is required to obtain the desired image beam waist. The criterion for the collimating lens is established by Eq. (46). From Eq. (39), the image beam waist needs to be greater than or equal to half the length of the detector; thus, it was chosen as $w_1 = 3\ mm$. The lens glass material was BK7 with $n_c = 1.5$. For the single-mode fiber, the object Gaussian beam waist is $w_0 = 2.5\ \mu m$. The focal length of the lens was solved using Eq. (46) to yield $f = 30.4\ mm$. It was subsequently substituted into Eq. (40) to determine the structural parameters of the lens. $R_1 = 9.6\ mm, R_2 = 24.6\ mm$ were chosen in this study as the structural parameters of the collimating lens.

4. Simulation verification and discussion

As shown in Fig. 7, the interrogation model developed in this study is simulated and verified using ZEMAX software. The pigtail and the LVF are placed at the object and image focus of the collimating lens, respectively. The distance between the detector and the LVF is *1* mm. The distance is intended to approximate the actual distance between the glass window and the pixel point of the line array image detector. The LVF structural parameters are listed in Table 2.

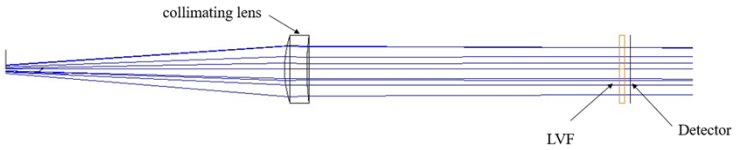

Fig. 7. Simulation layout in ZEMAX.

Figure 8 shows the intensity distribution of the transmitted light. The composite light is divided into seven bright stripes that are mutually separated. The stripes in the center are the brightest, whereas those on both sides are the darkest. The intensity of the stripes gradually decreases from the middle to both sides.

The LVF spectral transmittance function, T_{LVF}, was obtained by substituting the design parameters ($m = 4$, $N = 5$), operating range (*1505* nm-*1595* nm), and detector length $L = 6\ mm$ into Eqs. (15), (27), and (28).

Because the light reflected by the FBG sensors is a Gaussian beam, the relationship between the intensity distribution and the spot radius is as follows:

$$spa(x) = \exp(\frac{-(x - \frac{L}{2})^2}{w^2/2}) \tag{47}$$

where w is the spot radius. $w = 3\ mm$ was substituted into Eq. (47) to obtain the spatial light intensity distribution function, $spa(x)$. The Gaussian function with a wave peak width of *0.3* nm is used as the spectral function of the light reflected by the FBG sensors, $spec(\lambda_{FBG}, \lambda)$. The light intensity distribution of the transmitted light was obtained by introducing T_{LVF}, $spa(x)$, and $spec(\lambda_{FBG}, \lambda)$ into the interrogation model (Eq. (16)) developed in this study. Moreover, the calculated results were compared with the simulation results, which can be seen in Fig. 9. The

Optics EXPRESS

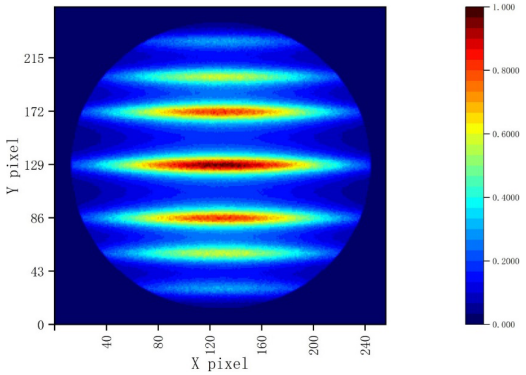

Fig. 8. Intensity distribution of transmitted light when the wavelengths of light reflected by FBG sensors are *1515* nm, *1525* nm, *1535* nm, *1550* nm, *1565* nm, *1575* nm, and *1585* nm in simulation. Detector pixel point arrangement is 256×256.

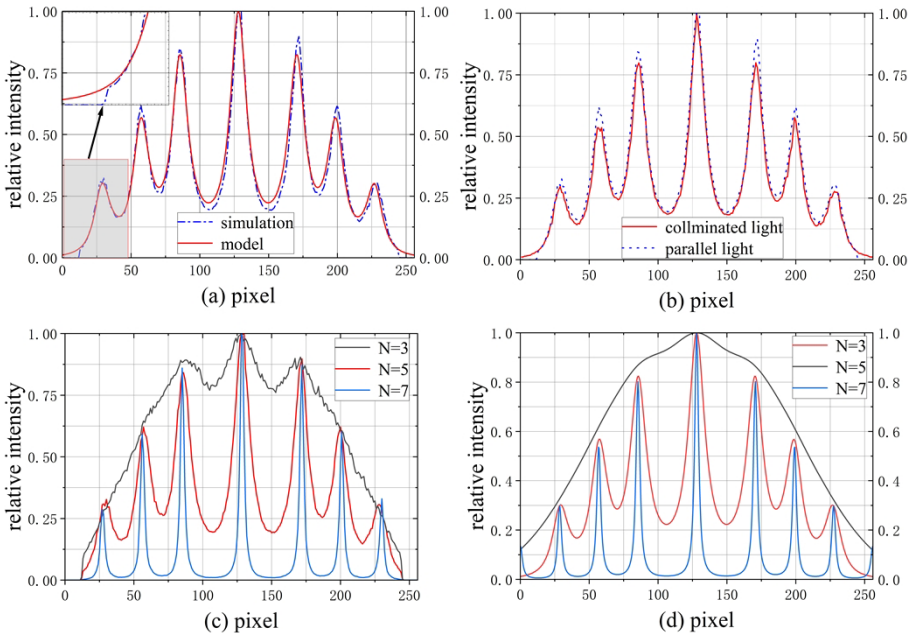

Fig. 9. (a) Results calculated using model and simulation; (b) Simulation results under collimated and parallel light, respectively; (c) Simulation results when $N = 3, 5, 7$; (d) Results calculated using model when $N = 3, 5, 7$.

Optics EXPRESS

model was calculated using MATLAB. The simulation results were obtained by extracting data from the middle column of the two-dimensional detector (see Fig. 8).

In Fig. 9(a), the wave peak widths and positions of the two curves coincide, indicating that the model results match the simulated results well. However, in Fig. 9(a), the wave peak width is *16* px, or *0.375* mm, which deviates from the design value of 0.3 mm. The light reflected by the FBG sensors is assumed to be monochromatic in the design of this study; however, in the simulation and the model, it is narrow band light with a bandwidth of *0.3* nm. Thus, the width of the wave peaks of the transmitted light increases. Consequently, the capacity of FBG sensors is reduced to 17.

In Fig. 9(a), when the pixel point is close to zero, the simulation light intensity decays rapidly, but the model decay is slower. Because of the presence of a diaphragm in the simulation, the light intensity at the boundary can rapidly decrease to zero. Moreover, because of the presence of the diaphragm, it is not possible to use the FBG sensors whose wavelengths are at the limits of the bandwidth range. This results in a further decrease in the capacity of the FBG sensors: $17 - 2 = 15$. Figure 10 shows the intensity distribution of the transmitted light in the simulation at the maximum capacity of *15*. Thirteen stripes of fifteen are visible in Fig. 10(a), the other two are too weak to be visible. However, fifteen wave peaks are clearly shown in Fig. 10(b). Because of the weakness of the wave peaks at the boundary, they may be affected by secondary wave peaks generated by neighboring wave peaks. For FBG sensors with a low side-mode suppressing ratio, the secondary wave peaks may be higher than the wave peaks at the boundary, thus, the wave peaks at the boundary cannot be interrogated successfully. Therefore, the FBG sensors used in our interrogator should have a high side-mode suppressing ratio to ensure a capacity of *15* FBG sensors.

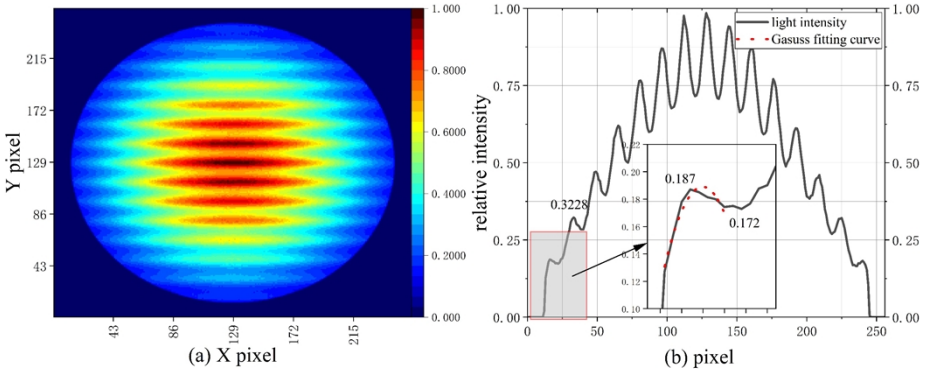

Fig. 10. (a) Intensity distribution of transmitted light on detector at maximum grating capacity. Detector pixel point arrangement is 256×256; (b) Intensity distribution in middle column of detector.

Figure 9(b) shows the distributions of the transmitted light intensity when the incident lights are collimated parallel lights, respectively. The width and position of the wave peak are nearly identical, indicating that the collimation effect of the collimating lens is comparable to that of the parallel light. This shows that the collimating lens designed in this study can meet the design requirements.

From Fig. 9(c), when $N = 3$, only three wave peaks located in the middle can be identified, whereas those at other positions cannot be identified because of the degradation phenomenon. The widths of the wave peaks are narrower at $N = 7$ than those at $N = 5$. Figure 9(d) shows the results of the model when $N = 3, 5, 7$. Comparing Fig. 9(c) and (d), the positions and widths of the wave peaks are consistent. This demonstrates that the model developed in this study is still in good agreement with the simulation when N is varied.

Optics EXPRESS

Figure 9(c) and (d) show that, for $N = 5, 7$, the width of the wave peaks differs, whereas their positions of the wave peaks remain consistent. This suggests that the positions of the wave peaks are independent of their widths. The minimum wavelength shift that an FBG sensor interrogation system can detect is its resolution. From the above analysis, it can be concluded that the resolution of the interrogation designed in this study is not limited by the width of the wave peaks, but only by the detector performance [26].

The detector of the interrogation system designed in this study was that of I-MON 256 OEM [32]. From the relevant manuals, it is known that the sampling errors of the detector follow a normal distribution, as expressed in the following equation.

$$dn \sim N(0, {U_n}^2) \tag{48}$$

where dn is the noise signal of the pixel, $N(\mu, \sigma^2)$ is a normal distribution with an expectation of μ and a variance of σ^2, U_n is the maximum value of the noise signal. In this study, U_n is 1 mV. A 1000 sets of detector sampling error data is generated according to the distribution as expressed in Eq. (48). The intensity of the transmitted light is obtained by substituting $\lambda_{FBG} = 1550\ nm$ into the interrogation model (Eq. (16)). The Gaussian fitting algorithm [33] is used to obtain the position of the wave peak of the transmitted light. The sampling error data and the intensity of the transmitted light are introduced into the Gaussian fitting algorithm and the results of the position of the wave peak are shown in Fig. 11.

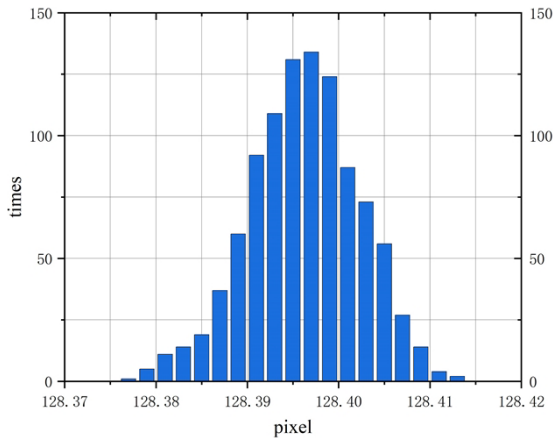

Fig. 11. Distribution of wave peak positions when considering noise. Wavelength of FBG sensor is 1550 nm.

Figure 11 shows that the results of 810 out of 1000 simulations are distributed between 128.389 and 128.403. Therefore, we can assume that there is at least an 80% probability that the experimental results are in 128.396 ± 0.007. By the relationship between the position of the wave peak and the wavelength of the light reflected by FBG sensors, we can get the resolution of the instrument as 2 pm.

5. Conclusion

By investigating the interrogation principles of LVF-based interrogation systems for FBG sensors, an interrogation model is established. By studying the ambiguity and degradation phenomenon of the multi-FBG sensor interrogation, the design criteria for the LVF are established. To ensure that the light reflected by the FBG sensors is incident vertically on the LVF and fully covers the detector, we define the design criteria for the collimating lens.

Optics EXPRESS

Overall, first, the design criteria established in this study can provide design guidance for an LVF-based FBG sensor interrogation system. The LVF-based FBG sensor interrogation system designed in this study has a bandwidth range of *90* nm (*1505* nm-*1595* nm), a resolution of less than *1* pm, and a capacity of *15* FBG sensors. It is a significant improvement over a previous design [30]. Second, the model agrees well with the simulation and can calculate the intensity distribution of the transmitted light accurately. This study can promote the application and development of an LVF-based FBG sensor interrogation system. In this study, the LVF-based FBG sensor interrogation system is small, light, and highly vibration-resist. Furthermore, it can meet the requirements for aviation instruments, overcome the limitations of FBG sensor applications, and thus, optimize an aviation monitoring system and prevent aircraft safety accidents.

However, the design criteria of the capacity of FBG sensors developed in this study ignore the spectral bandwidth of the light reflected by the FBG sensors. Thus, the capacity in the simulation deviates slightly from the capacity in the design. For a DBR, the reflection phase is related to the incident light wavelength, which will cause the wave peak shift of the transmitted light. However, this study assumes that the reflection phase is zero and ignores this factor. Furthermore, the nonlinear variation in the thickness of the resonant cavity layer of the LVF in the actual preparation environment is not considered. These elements will be considered in the next stage of the prototype preparation study.

Funding. Research Program of Sanya Yazhou Bay Science and Technology City under Grant (009, 01, 2020, SKJC); Technology Development Research Project of China Nuclear Power Co. (A19056, LTD); Shaoxing 'Home of Celebrities' Talent Program.

Disclosures. The authors declare no conflicts of interest.

Data availability. Data underlying the results presented in this paper are not publicly available at this time but may be obtained from the authors upon reasonable request.

References

1. T. K. Gangopadhyay, "Prospects for Fiber Bragg Gratings and Fabry-Perot Interferometers in fiber-optic vibration sensing," Sens. Actuators, A **113**(1), 20–38 (2004).
2. L. Teng, L. Feng, H. Lin, B. Zhang, and C. Liu, "A new fiber Bragg grating accelerometer," in *Sixth International Symposium on Instrumentation and Control Technology: Signal Analysis, Measurement Theory, Photo-Electronic Technology, and Artificial Intelligence* (SPIE, 2006), Vol. 6357, pp. 937–942.
3. F. Urban, J. Kadlec, R. Vlach, and R. Kuchta, "Design of a Pressure Sensor Based on Optical Fiber Bragg Grating Lateral Deformation," Sensors **10**(12), 11212–11225 (2010).
4. M. Song, S. B. Lee, S. S. Choi, and B. Lee, "Simultaneous Measurement of Temperature and Strain Using Two Fiber Bragg Gratings Embedded in a Glass Tube," Opt. Fiber Technol. **3**(2), 194–196 (1997).
5. R. Hypszer and H. J. Wierzba, "Fiber optic technique for relative humidity sensors," in *Optoelectronic and Electronic Sensors II* (SPIE, 1997), Vol. 3054, pp. 145–150.
6. T. H. T. Chan, L. Yu, H. Y. Tam, Y. Q. Ni, S. Y. Liu, W. H. Chung, and L. K. Cheng, "Fiber Bragg grating sensors for structural health monitoring of Tsing Ma bridge: Background and experimental observation," Eng. Struct. **28**(5), 648–659 (2006).
7. H. Song, K. Kim, and J. Lee, "Development of optical fiber Bragg grating force-reflection sensor system of medical application for safe minimally invasive robotic surgery," Rev. Sci. Instrum. **82**(7), 074301 (2011).
8. A. Ghoshal, J. Ayers, M. Gurvich, M. Urban, and N. Bordick, "Experimental investigations in embedded sensing of composite components in aerospace vehicles," Composites, Part B **71**, 52–62 (2015).
9. E. Verstrynge, K. De Wilder, A. Drougkas, E. Voet, K. Van Balen, and M. Wevers, "Crack monitoring in historical masonry with distributed strain and acoustic emission sensing techniques," Constr. Build. Mater. **162**, 898–907 (2018).
10. M. Ciminello, N. D. Boffa, A. Concilio, V. Memmolo, E. Monaco, and F. Ricci, "Stringer debonding edge detection employing fiber optics by combined distributed strain profile and wave scattering approaches for non-model based SHM," Compos. Struct. **216**, 58–66 (2019).
11. G. Yan, T. Wang, L. Zhu, F. Meng, and W. Zhuang, "A novel strain-decoupled sensitized FBG temperature sensor and its applications to aircraft thermal management," Opt. Laser Technol. **140**, 106597 (2021).
12. B. Jiang, J. Zhao, C. Qin, Z. Huang, and F. Fan, "An optimized strain demodulation method based on dynamic double matched fiber Bragg grating filtering," Opt. Lasers Eng. **49**(3), 415–418 (2011).
13. S.-Y. Jeong, S.-J. Choi, and J.-K. Pan, "An Implementation of FBG Interrogator with a Tunable Fabry-Perot Filter," in *Advanced Photonics (IPR, NOMA, Sensors, Networks, SPPCom, PS)* (Optica Publishing Group, 2017), paper JTu4A.16.

Optics EXPRESS

14. K. Ogawa, S. Koyama, Y. Haseda, K. Fujita, H. Ishizawa, and K. Fujimoto, "Wireless, Portable Fiber Bragg Grating Interrogation System Employing Optical Edge Filter," Sensors **19**(14), 3222 (2019).
15. B. Das and V. Chandra, "Fiber-MZI-based FBG sensor interrogation: comparative study with a CCD spectrometer," Appl. Opt. **55**(29), 8287–8292 (2016).
16. T. C. Buck, M. S. Müller, A. Perez Grassi, and A. W. Koch, "Detection of aliasing in sampled dynamic fiber Bragg grating signals recorded by spectrometers," Measurement **44**(6), 1053–1058 (2011).
17. Y. S. Borisov, A. M. Nizametdinov, O. V. Ivanov, and A. A. Chertoriyskiy, "Measurement of spectra of fiber Bragg gratings by tuning the wavelength of a laser diode," Opt. Laser Technol. **151**, 108048 (2022).
18. J. Liu, L. Zhu, W. He, Y. Wang, F. Meng, and Y. Song, "Fiber grating sensing interrogation system based on a modulated grating Y-branch tunable laser for core-and-cladding-integrated fiber Bragg grating temperature measurement," Rev. Sci. Instrum. **91**(1), 014904 (2020).
19. A. Emadi, H. Wu, G. de Graaf, and R. Wolffenbuttel, "Design and implementation of a sub-nm resolution microspectrometer based on a Linear-Variable Optical Filter," Opt. Express **20**(1), 489 (2012).
20. A. Emadi, H. Wu, G. de Graaf, P. Enoksson, J. H. Correia, and R. Wolffenbuttel, "Linear variable optical filter-based ultraviolet microspectrometer," Appl. Opt. **51**(19), 4308–4315 (2012).
21. B. Sheng, P. Chen, C. Tao, R. Hong, Y. Huang, and D. Zhang, "Linear variable filters fabricated by ion beam etching with triangle-shaped mask and normal film coating technique," Chin. Opt. Lett. **13**(12), 122301 (2015).
22. A. Piegari, J. Bulir, and A. K. Sytchkova, "Variable narrow-band transmission filters for spectrometry from space. 2. Fabrication process," Appl. Opt. **47**(13), C151–C156 (2008).
23. A. Piegari and J. Bulir, "Variable narrowband transmission filters with a wide rejection band for spectrometry," Appl. Opt. **45**(16), 3768 (2006).
24. L. Gao and L. V. Wang, "A review of snapshot multidimensional optical imaging: Measuring photon tags in parallel," Phys. Rep. **616**, 1–37 (2016).
25. O. Schmidt, P. Kiesel, S. Mohta, and N. M. Johnson, "Resolving pm wavelength shifts in optical sensing," Appl. Phys. B **86**(4), 593–600 (2007).
26. R. Wuchrer and T. Härtling, "Filter-based interrogation unit for optical wavelength shift sensors," in *Smart Sensor Phenomena, Technology, Networks, and Systems Integration 2013* (SPIE, 2013), Vol. 8693, pp. 25–29.
27. R. Wuchrer, G. Lautenschlager, R. Metasch, M. Rollig, T. Fleischer, and T. Hartling, "Filter-based interrogation of fiber Bragg grating sensors," in *Proceedings of the 2014 37th International Spring Seminar on Electronics Technology* (IEEE, 2014), pp. 453–457.
28. P. Ji, C.-S. Park, S. Gao, S.-S. Lee, and D.-Y. Choi, "Angle-tolerant linear variable color filter based on a tapered etalon," Opt. Express **25**(3), 2153 (2017).
29. C. Williams, G. Rughoobur, A. J. Flewitt, and T. D. Wilkinson, "Single-step fabrication of thin-film linear variable bandpass filters based on metal–insulator–metal geometry," Appl. Opt. **55**(32), 9237 (2016).
30. P. Kiesel, O. Schmidt, S. Mohta, N. Johnson, and S. Malzer, "Compact, low-cost, and high-resolution interrogation unit for optical sensors," Appl. Phys. Lett. **89**(20), 201113 (2006).
31. H. A. MacLeod, *Thin-Film Optical Filters*, 4th ed. (CRC Press, 2010).
32. Ibsen Photonics A/S, "I-MON OEM," https://ibsen.com/products/interrogation-monitors/i-mon-oem.
33. Y. Chen, L. Chen, H. Liu, and K. Wang, "Research on FBG sensor signal wavelength demodulation based on improved wavelet transform," Optik **124**(21), 4802–4804 (2013).